PHYSICAL REVIEW C VOLUME 53, NUMBER 2 FEBRUARY 1996

# Resonant structures in the $^{20}$Ne+$^{16}$O system

Y. Miao, R. W. Zurmühle, S. P. Barrow, N. G. Wimer, J. T. Murgatroyd,* C. Lee,† and Z. Liu
*Department of Physics and Astronomy, University of Pennsylvania, Philadelphia, Pennsylvania 19104*

(Received 6 October 1995)

In a search for high spin molecular states in $^{36}$Ar, the $^{20}$Ne+$^{16}$O system was studied using a differentially pumped windowless $^{20}$Ne gas target. Angle-averaged excitation functions for the $^{20}$Ne+$^{16}$O and $^{24}$Mg+$^{12}$C mass partitions were obtained for the energy range 16.39 MeV $\leq E_{\mathrm{c.m.}} \leq$ 41.67 MeV in 278 keV steps. Inelastic scattering involving the $^{16}$O($0_2^+$, 6.05 MeV) state was separated from the nearby $^{16}$O($3_1^-$, 6.13 MeV) state by detecting the $e^-$ and $e^+$ emitted from the internal pair decay of the $^{16}$O($0_2^+$) state. A statistical fluctuation analysis indicates that several correlated structures are present in the current system. Tentative spin assignments based on angular distribution measurements suggest the resonant structures could be associated with rotational states of $^{36}$Ar. The results are compared with a cranked cluster model calculation.

PACS number(s): 25.70.Ef, 25.70.Hi

## I. INTRODUCTION

Ever since evidence of highly deformed excited high spin states in $^{48}$Cr was first observed in the $^{24}$Mg+$^{24}$Mg system [1,2], much interest has been focused on other similar systems, for example, $^{20}$Ne+$^{20}$Ne [3], $^{20}$Ne+$^{24}$Mg, and $^{20}$Ne+$^{28}$Si [4]. Earlier studies of the $^{20}$Ne+$^{16}$O system revealed some correlated structures in the excitation functions of the $^{20}$Ne+$^{16}$O reaction [5,6]. In those investigations, single-angle excitation functions were measured for the elastic and low-lying states of $^{20}$Ne inelastic scattering, as well as angular distributions at several beam energies. The study of the $^{24}$Mg+$^{12}$C reaction, which is the same compound system, also showed resonant structures [7] in the form of broad resonances in three channels: the inelastic excitations of $^{24}$Mg, and the $2\alpha$ and $\alpha p$ fusion-evaporation channels. These are the channels most sensitive to the grazing entrance channel partial waves. Resonances in the $^{24}$Mg($^{12}$C,$\alpha$)$^{32}$S reaction also appear to be due to the same states that contribute to the $^{24}$Mg+$^{12}$C channel. A cranked $\alpha$-cluster model calculation using the Brink-Boeker $B1$ nucleon-nucleon interaction predicted a superdeformed rotational band in $^{36}$Ar with a 3:1 axis ratio deformation [8]. Both $^{36}$Ar and $^{48}$Cr are ‘‘doubly magic’’ nuclei at the large deformations considered here, and it is not unreasonable to consider these calculated states in $^{36}$Ar as analogs of the calculated superdeformed states in $^{48}$Cr obtained with the same formalism. The mass density distribution calculated for these superdeformed states suggests a large overlap with $^{16}$O-$\alpha$-$^{16}$O and $^{16}$O-$^{20}$Ne fission decay channels. Similar calculations suggest superdeformed excited states for several other $4N$ nuclei [9]. Previously, this model has been used very successfully in studies of lighter systems with total mass less than $^{24}$Mg [10]. These experimental and theoretical studies raise the possibility of highly deformed molecular states in $^{36}$Ar, and the current work presents a detailed discussion of recent measurements to determine the existence of such resonances in the $^{16}$O-$^{20}$Ne system.

In order to investigate the contribution of compound nucleus formation to the $^{20}$Ne+$^{16}$O system, it is essential to acquire angle-integrated cross sections, because this reduces the likelihood that any observed structures are the result of angular distribution effects generated by interference between amplitudes of several spin values. In the current work, we measured angle-averaged excitation functions for elastic and inelastic scattering of $^{20}$Ne+$^{16}$O and for $^{20}$Ne($^{16}$O, $^{12}$C*)$^{24}$Mg* reactions as well. Excitation functions for several exit channels that populate the $0_2^+$(6.05 MeV) state of $^{16}$O are presented for the first time in this work. The large prolate deformation of this excited state may be favored in the decay of the highly deformed states in $^{36}$Ar. For example, a study of the spins of the gross resonances in the $^{16}$O($^{16}$O, $^{16}$O(g.s.))$^{16}$O($0_2^+$) reaction [11] determined that the spins of these resonances are larger than those derived from optical model calculations for resonances in the elastic channel at comparable energies. The large angular momentum mismatch in the $0_2^+$(6.05 MeV) decay channels suppresses the cross section of direct processes and favors the observation of highly deformed resonant states. In addition, one advantage of studying zero intrinsic spin exit channels is that it is a more straightforward process to extract spin assignments from angular distribution measurements than for nonzero spin exit channels. In our measurements, unique identification of the $0_2^+$ exit channels has been accomplished by detecting the $e^-$ and $e^+$ emitted from the internal pair decay of the $^{16}$O($0_2^+$) state, which is unresolved from the $^{16}$O($3_1^-$) state by kinematic reconstruction techniques alone. The $e^-$–$e^+$ pair yield is directly proportional to the total $0_2^+$ cross section since the contribution from internal pair conversion of $3_1^- \rightarrow 0_1^+$ $\gamma$ transition is negligible.

Section II of this work begins with a brief discussion of the experimental setup, including the differentially pumped windowless $^{20}$Ne gas target system. The data reduction is also presented in this section. In Sec. III the experimental results are presented. The statistical analysis and discussion of the results are in Sec. IV, Sec. V summarizes this work.

## II. EXPERIMENT

A differentially pumped windowless $^{20}$Ne gas target was used. A schematic of the gas target apparatus is shown in Fig.

---

*Present address: Wayne State University, Detroit, MI, 48202.

†Present address: Florida State University, Tallahassee, FL, 32306.

0556-2813/96/53(2)/815(8)/$06.00

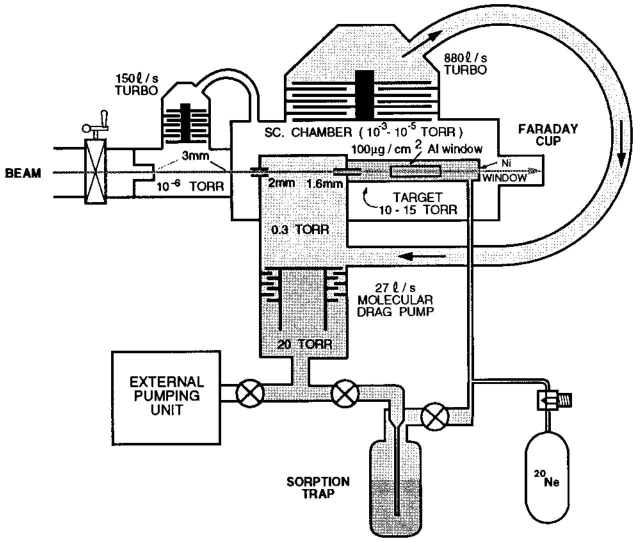

FIG. 1. Schematic of the differentially pumped $^{20}$Ne gas target vacuum system perpendicular to the reaction plane, not to scale.

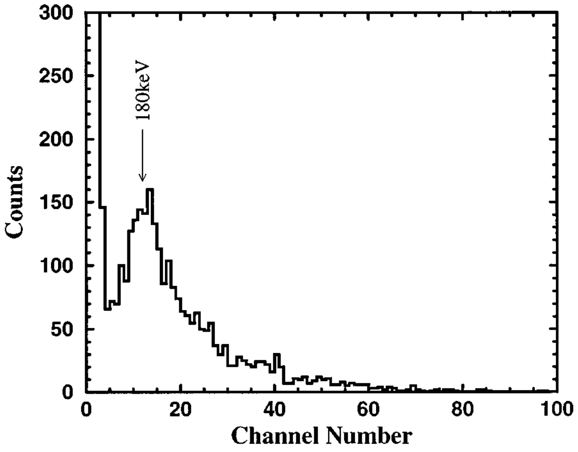

FIG. 2. A typical $e^-$ and $e^+$ energy spectrum.

1. There are four collimators which define four pressure regions inside the vacuum system. The diameter of the collimators increases with the distance from the target region, from 1.6 mm to 3.0 mm, in order to allow good beam transmission to the target area. The narrowest collimator restricts the flow of gas out of the target cell, and during measurements the beam is steered into the target region such that the beam waist is minimized at this collimator. The windowless entrance of the target cell allowed the beam to enter it with little energy degradation prior to reaching the target region. Two additional cylindrical collimators inside the gas cell, not shown in Fig. 1, are spaced by 1 cm and define the event region, i.e., the region seen by the detectors. The pressure in the target region was typically around 10 torr during the experiment or 11 $\mu$g/cm$^2$, which corresponds to an energy loss of roughly 50 keV for the beam energies studied in this work. For this experiment the gas cell and inner collimators were built from thin aluminum in order to minimize the sensitivity of our setup to the 6.13 MeV $\gamma$ decay from the nearby $3_1^-$ state of $^{16}$O. The largest source of this sensitivity is the conversions of $\gamma$ rays into energetic electrons in the materials surrounding the gas. This setup was slightly modified from the original design, in which tantalum was used for these collimators [3,4]. In the recoil plane of the detectors, two nearly rectangular windows, each 1.62 cm×0.64 cm, were cut into the gas target housing. They were covered with $^{27}$Al foils, with typical thicknesses ranging from 75 to 100 $\mu$g/cm$^2$. These foils make it possible for the reactants to escape the event region while confining the $^{20}$Ne gas. The typical total energy loss in these foils for the decay fragments studied in this work was approximately 1 MeV. The $^{20}$Ne gas that exits the target region through the 1.6 mm collimator was collected by a molecular drag pump and purified by a sorption pump before being reintroduced back into the target region. This recycling process enabled us to maintain a stable pressure with a fixed amount of circulating gas during the runs. A 500 $\mu$g/cm$^2$ nickel foil downstream of the event region served as the beam exit window. The beam continues through the nickel foil and into a Faraday cup, which integrates the total charge of the fully stripped beam nuclei for normalization purposes. The rest of the volume of the scattering chamber shown in Fig. 1 is maintained at very good vacuum, typically $1\times10^{-5}$ torr. For the purpose of differentially pumping, two turbomolecular pumps, with pumping speeds of 880 l/s and 150 l/s, are mounted directly to the scattering chamber but are electrically insulated from the chamber and the detectors mounted inside. Isotropically enriched $^{20}$Ne gas was used as the target gas.

The recoil fragments were detected by two large-area, low-resistivity surface barrier detectors positioned on each side of target relative to the beam, and centered at $\pm 44°$ for the excitation function measurements. A 500-$\mu$m-thick ion-implanted silicon detector [12] with a 4 cm×6 cm surface area that was divided into seven segments was used to detect the electrons from the decay of the $0_2^+$(6.05 MeV) state of $^{16}$O. This detector was positioned 1.8 cm from the center of the target region, parallel to the reaction plane defined by the two heavy ion detectors. A typical $e^-$ and $e^+$ energy spectrum from the electron detector is shown in Fig. 2. The peak represents the minimum ionizing energy for this detector thickness.

The $^{16}$O beam was provided by the University of Pennsylvania Tandem Laboratory accelerator. Standard recoil coincidence techniques were used in this measurement. In addition to the energy information, the time-of-flight (TOF) difference of every coincidence event was also measured. For any binary decay reaction, the energy signals of the two fragments, combined with the TOF information, provides sufficient information to reconstruct the various mass partitions in the exit channels, as well as the center-of-mass angle $\theta_{\mathrm{c.m.}}$ for each event. A typical exit channel mass partition spectrum ($\Delta T$) is shown in Fig. 3. Only events with $Q$ values greater than $-22$ MeV were included in the figure. The mass partition for each peak is labeled in the figure. The central peak was determined to be a combination of $^{16}$O+$^{16}$O+$\alpha$ and $^{18}$F+$^{18}$F decays [13]. The results of the $^{18}$F+$^{18}$F channel will not be discussed in this paper; the interested reader is referred to Ref [13]. The $Q$ spectra for the $^{20}$Ne+$^{16}$O and $^{24}$Mg+$^{12}$C mass partitions are shown in Fig. 4. Figure 4(a) shows the $Q$ spectrum for the mass partition

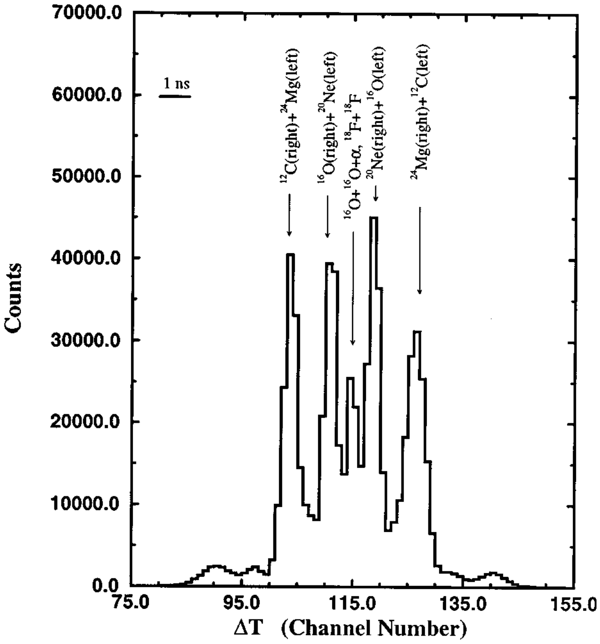

FIG. 3. The mass partitions as determined by the time of flight ($\Delta T$).

$^{20}$Ne+$^{16}$O, while Fig. 4(b) shows the same spectrum with an additional electron detector coincidence requirement. The peaks other than the excitations of the $^{16}$O($0_2^+$) state are due to the $\gamma$ ray sensitivity of the system, since false coincidences from the electron detector background were subtracted from this spectrum. The estimated conversion rate of $\gamma$ decay from the $3_1^-$ state is about 0.2%–0.4% for our experimental setup. Figure 4(c) plots a typical $Q$ spectrum for the $^{24}$Mg+$^{12}$C mass partition. From these $Q$ spectra it is evident that the energy resolution of peaks is about 550 keV full width at half the maximum (FWHM), and is sufficient to resolve low-lying excited states. The solid angle of the heavy ion recoil coincidence was calculated using the Monte Carlo technique, as the spatial extent of the gas target over 1 cm in length makes it difficult to calculate the solid angle directly. The efficiency of the electron detector was also estimated using the Monte Carlo technique, as direct measurement of the electron detector efficiency for the $0_2^+$ state of $^{16}$O is difficult in the current experimental setup, as it is for other similar studies [14,15].

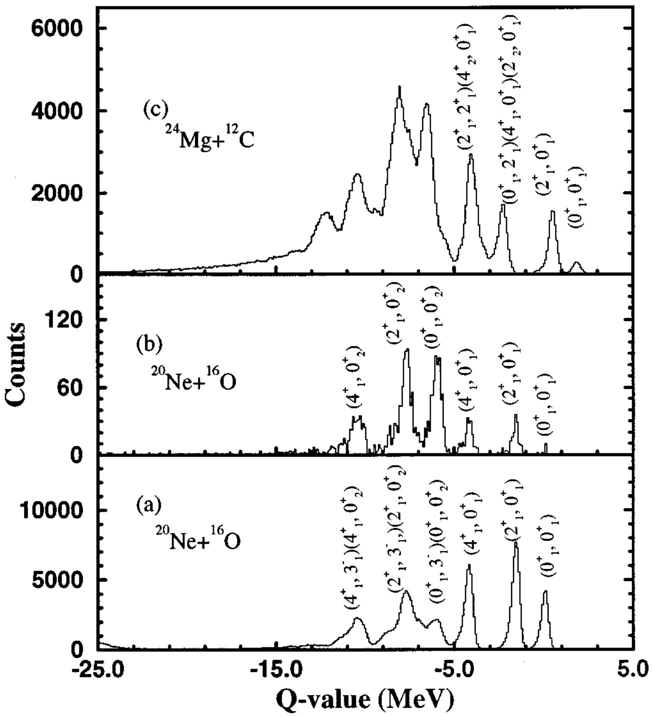

FIG. 4. The $Q$ spectra for the $^{20}$Ne+$^{16}$O system. (a) and (b) are for $^{20}$Ne+$^{16}$O, with (b) requiring the additional constraint of an electron detector coincidence, and (c) is for $^{24}$Mg+$^{12}$C mass partition.

For the angular distribution measurements, the center-of-mass angle $\theta_{\text{c.m.}}$ was reconstructed from the kinematical relation

$$\cos\theta_{\text{c.m.}}=\frac{(E_l-E_r)+(Q+E_b)\dfrac{M_l-M_r}{M_l+M_r}+\left(1-\dfrac{2M_l}{M_p+M_t}\right)\dfrac{2M_pE_b}{M_p+M_t}}{\dfrac{4M_p}{M_l+M_r}\sqrt{\dfrac{M_tE_b}{M_p+M_t}+Q}\sqrt{\dfrac{M_lM_rE_b}{M_p(M_l+M_r)}}}, \tag{1}$$

where $E_l$ and $E_r$ are the energy signals recorded by the left and right detectors, respectively, $E_b$ and $Q$ are the beam energy and $Q$ value of the reaction, and $M_l$, $M_r$, $M_p$, and $M_t$ are the masses of the left, right, projectile, and target particles, respectively. The energy losses of the exiting fragments in the $^{27}$Al foils affect the accuracy of this calculations. However, the term $(E_l-E_r)$ used in this formula greatly reduced the dependence on energy losses for decay fragments with comparable masses at the angle ranges considered in this work, since the energy losses in the foils are so similar. For example, in the case of $^{20}$Ne+$^{16}$O elastic scattering at a beam energy of 36 MeV, the calculated angle yields a discrepancy of 0.3° from the actual angle for $\theta_{\text{c.m.}}=96°$.

### III. EXPERIMENTAL RESULTS

Angle-integrated excitation functions for elastic and inelastic scattering of the $^{20}$Ne+$^{16}$O system have been measured in the energy range from 16.1 MeV $\leqslant E_{\text{c.m.}} \leqslant$ 41.7 MeV with a step size $\Delta E=278$ keV. In these measurements eight inelastic channels have been identified with $Q$ values

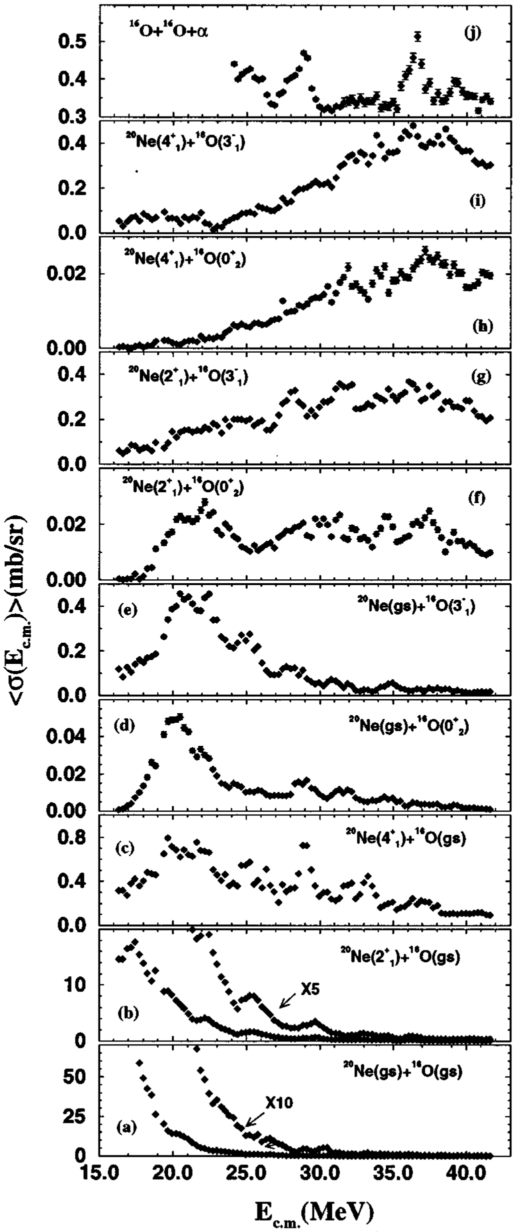

FIG. 5. Excitation functions for the elastic and inelastic scattering of $^{20}$Ne+$^{16}$O. The arrows in (a) and (b) indicate excitation functions for those two exit channels in which the vertical scale has been multiplied by the amount shown in the figure.

ranging from $-10.36$ MeV to $-1.63$ MeV. The cross sections for the elastic channel are averaged over the angle range $64° \leqslant \theta_{\text{c.m.}} \leqslant 106°$. The excitation functions are shown in Figs. 5(a)–5(i); the error bars represent statistical uncertainties. Resonant structures are present in most of these channels, with widths varying from several hundred keV to roughly 2 MeV. Resonances centered at $E_{\text{c.m.}}=25.0$ and 28.9 MeV are observed in the four lowest excitation exit channels. The overall cross section of the $^{20}\text{Ne}+{}^{16}\text{O}(0_2^+)$ channel is roughly one order of magnitude smaller than that of the nearby $^{20}\text{Ne}+{}^{16}\text{O}(3_1^-)$ channel, presumably due to angular momentum mismatch with the entrance channel. A gross structure is centered at $E_{\text{c.m.}}=20$ MeV in the $^{20}\text{Ne}+{}^{16}\text{O}(0_2^+)$ channel with a peak-to-background ratio of 3.3:1.

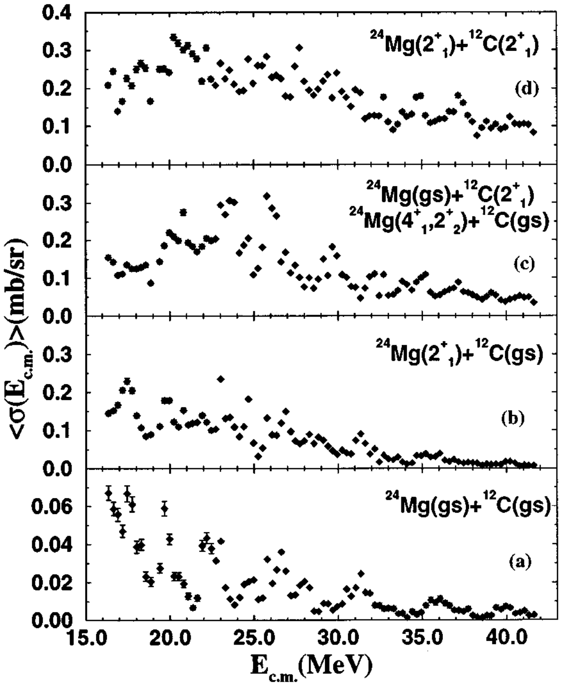

FIG. 6. Excitation functions for the $^{20}\text{Ne}({}^{16}\text{O},{}^{12}\text{C})^{24}\text{Mg}$ reactions.

Because of the large negative $Q$ value of this channel, the exiting kinetic energy is comparable to the Coulomb barrier energy for this resonance. There is little evidence that correlated structures exist in the excitation functions for higher excitations of these two nuclei. Figure 5(j) is the excitation function of the three-body final state $^{16}\text{O}+{}^{16}\text{O}+\alpha$. The overall cross sections of this channel are the same order as the inelastic scattering reactions, and it is reasonable to assume that the $^{16}\text{O}+{}^{16}\text{O}+\alpha$ channel observed in this work is an inelastic scattering process in which the $^{20}$Ne fragment populates an $\alpha$-unbound excited state ($E_\alpha=4.7$ MeV), which subsequently decays by $\alpha$ emission. The structure centered at $E_{\text{c.m.}}=28.9$ MeV in Fig. 5(j) is also seen in several other low-lying inelastic channels.

The results of the angle-integrated excitation function for the $^{20}\text{Ne}({}^{16}\text{O},{}^{24}\text{Mg})^{12}\text{C}$ reactions are plotted in Fig. 6. All four excitation functions display a high density of structures across the entire energy range, and some of them are as narrow as several hundred keV, especially at lower energies. The most pronounced structures appear in the (g.s.,g.s.) excitation function for $E_{\text{c.m.}}<30$ MeV. Narrow structures are centered at $E_{\text{c.m.}}=17.5$, 19.7, 22.4, 23.1, 24.7, and 25.8 MeV. The structures at $E_{\text{c.m.}}=23.1$, 24.7, and 25.8 MeV are seen in all four channels.

Angular distributions were measured at several energies for both the $^{20}\text{Ne}+{}^{16}\text{O}$ and $^{24}\text{Mg}+{}^{12}\text{C}$ mass partitions. Figures 7(a)–7(c) show angular distributions for $^{20}\text{Ne(g.s.)}+{}^{16}\text{O(g.s.)}$ and Figs. 7(d)–7(f) for $^{20}\text{Ne(g.s.)}+{}^{16}\text{O}(0_2^+)$ at $E_{\text{c.m.}}=20.0$, 23.9, and 28.9 MeV. The data at $E_{\text{c.m.}}=23.9$ MeV are an off-resonance measurement. A clear backward rise in the elastic cross sections suggests that elastic $\alpha$ transfer dominates the cross sections for angles larger than 100°. The results of optical model (OM) and distorted wave

TABLE I. Optical model parameters used for the $^{20}$Ne+$^{16}$O elastic channel.

| $E_{\mathrm{c.m.}}$ (MeV) | $V_0$ (MeV) | $r_R$ (fm) | $a_R$ (fm) | $W_0$ (MeV) | $r_I$ (fm) | $a_I$ (fm) | $l_{\mathrm{gr}}(\hbar)$ |
|---|---|---|---|---|---|---|---|
| 20.00 | 63.00 | 1.18 | 0.59 | 6.50 | 1.00 | 0.32 | 14–15 |
| 23.89 | 60.50 | 1.18 | 0.59 | 12.00 | 1.00 | 0.32 | 17–18 |
| 28.89 | 55.00 | 1.18 | 0.59 | 26.00 | 1.00 | 0.32 | 20–21 |

Born approximation (DWBA) $\alpha$-transfer calculations are compared with the elastic scattering angular distributions in these figures; the dashed lines are the results from optical model calculations [16], and the solid lines are the results from coherent sums of OM+DWBA calculations using the computer code DWUCK5 [17]. The standard Woods-Saxon optical potential was used in these calculations, and the parameters are listed in Table I. The grazing angular momenta for the entrance channel are also listed. The optical model parameters were arrived at by requiring good agreement between the fits and the angular distributions for the most forward angles in the OM calculations and for the backward angles in the OM+DWBA calculations. The real part of the Woods-Saxon potential was used to calculate the cluster form factor in the DWBA amplitude. The radius and diffuseness parameters of the Woods-Saxon well were taken as $r_0$=1.4 fm and $a$=0.65 fm, and the $\alpha$-spectroscopic factor used for the transfer reaction calculations was $S_\alpha$=0.8 [18]. The angular distribution at $E_{\mathrm{c.m.}}$=23.89 MeV [Fig. 7(b)] is assumed to be dominated by direct reaction processes since it is an off-resonance measurement. The OM cross section for this energy shows good agreement with the data at forward angles, but it deviates significantly from the data at larger angles, and the oscillations in the cross sections are also out of phase with the data. The rise in the cross section at large angles and the oscillations for $\theta_{\mathrm{c.m.}}>110°$ are well reproduced by the OM + DWBA calculation, as are the oscillations in the intermediate region where the two processes are comparable. The angular distribution at $E_{\mathrm{c.m.}}$=20.0 MeV is dominated by elastic scattering over the entire angle range being measured, since the OM results are in qualitative agreement with the data up to $\theta_{\mathrm{c.m.}}=120°$. The experimental cross sections are underestimated in the calculations for $E_{\mathrm{c.m.}}$=28.9 MeV, although the average slope is correctly predicted. The data for $\theta_{\mathrm{c.m.}}>80°$ display oscillatory behavior with a fairly constant peak intensity over a large angle range, in a manner consistent with a single dominant partial wave. A fit to $|a_{19}P_{19}(\cos\theta)|^2$ is shown by the dotted line in this figure, which reproduces the oscillations in the experimental cross section well. The angular distributions for inelastic scattering to $^{20}$Ne(g.s.)+$^{16}$O($0_2^+$) are shown in Figs. 7(d)–7(f), along with fits to the single partial waves $l$=6 at $E_{\mathrm{c.m.}}$=20.0 MeV and $l$=19 at $E_{\mathrm{c.m.}}$=28.89 MeV. The oscillations in those cross sections are well reproduced, suggesting strong contributions from $l$=6 and $l$=19 for the resonances at these two energies. The $l$ value for the $E_{\mathrm{c.m.}}$=28.9 MeV resonance is the same as that obtained from the elastic channel. The results of the fits are summarized in Table II. The relatively large values of the reduced $\chi^2$ may come from background contributions.

Angular distributions of the $^{20}$Ne($^{16}$O, $^{12}$C(g.s.)) $^{24}$Mg(g.s.) reaction have been measured at the energies $E_{\mathrm{c.m.}}$=17.5, 19.7, 22.4, 23.1, 24.7, and 25.8 MeV. Pronounced peaks were centered on all of these energies for the mutual ground state transition. Figure 8 shows the angular distributions at these energies, along with the results of fits to $P_l^2(\cos\theta)$ plotted with solid curves for $l$=10, 12, 15, 15, 17, and 17 for $E_{\mathrm{c.m.}}$=17.5, 19.7, 22.4, 23.1, 24.7, and 25.8 MeV, respectively. All angular distributions display pronounced oscillatory structures, and the shapes of the oscillations can be reproduced reasonably well by a single partial wave, with a few exceptions such as $E_{\mathrm{c.m.}}$=23.1 and 24.7 MeV. The fits suggest that the plotted Legendre polynomials may be the dominant partial waves for these resonances, even though it

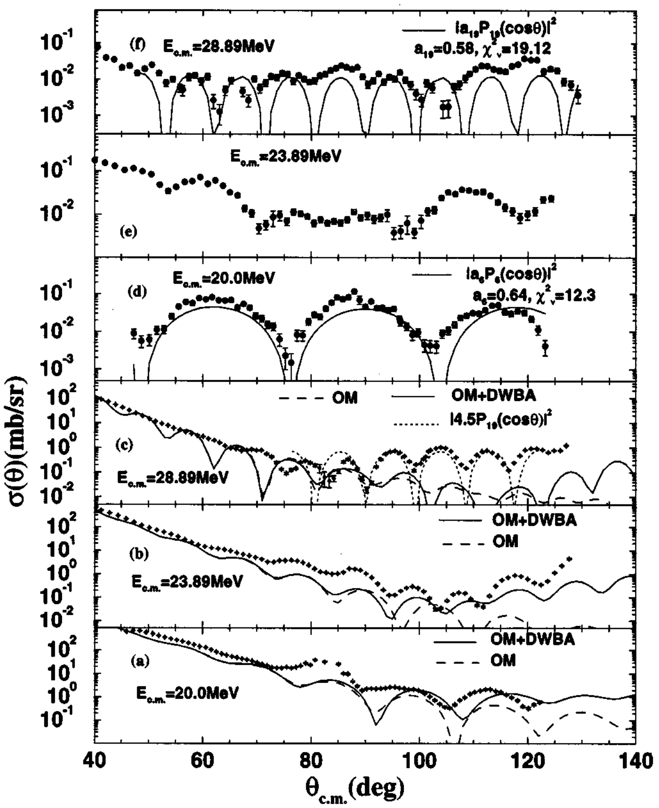

FIG. 7. Angular distributions for the elastic (a)–(c) and ($0^+$, $0_2^+$) inelastic (d)–(f) channels at $E_{\mathrm{c.m.}}$=20.0, 23.9, and 28.9 MeV.

TABLE II. Least squares fitting parameters for $|a_l P_l(\cos\theta)|^2$.

| $E_{\mathrm{c.m.}}$(MeV) | $l$ | $a_l$ | $\chi^2_\nu$ |
|---|---|---|---|
| 20.00 | 6 | 0.64 | 12.30 |
| 28.89 | 19 | 0.58 | 19.12 |

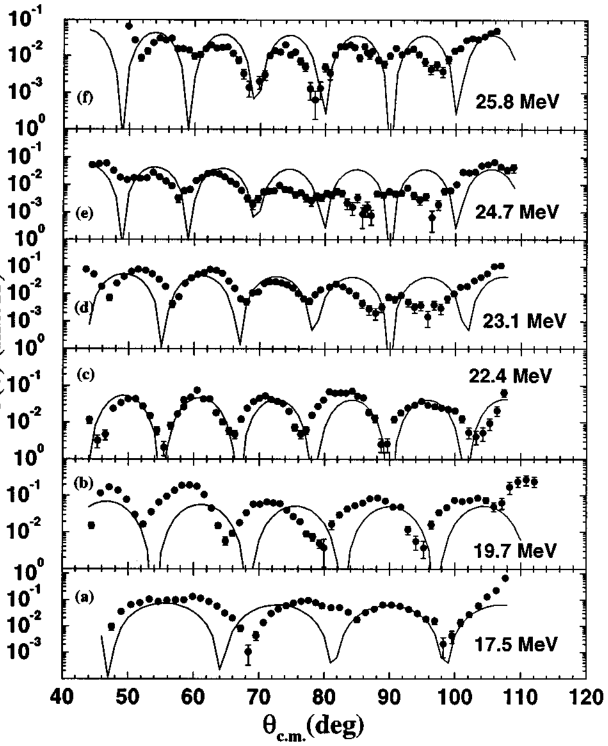

FIG. 8. Angular distributions for the mutual ground state $^{20}$Ne($^{16}$O,$^{12}$C)$^{24}$Mg transitions. The solid lines are $|P_l(\cos\theta)|^2$ with $l$ = 10, 12, 15, 15, 17, and 17 for $E_{\mathrm{c.m.}}$ = 17.5, 19.7, 22.4, 23.1, 24.7, and 25.8 MeV, respectively.

appears that more than one partial wave contributes strongly to some of these resonances. These $l$ values are very close to the grazing angular momenta of the entrance channel obtained from the optical model parameters listed in Table I. The resonance at $E_{\mathrm{c.m.}}=24.7$ MeV was previously reported in Ref. [6], in which the resonating partial wave was determined to be $l=18$, while another study suggested that $l=17$ was the dominate partial wave [5]. Our data illustrate that more than one partial wave may have appreciable contributions.

## IV. ANALYSIS AND DISCUSSION

The excitation functions indicate that the highest density of structures is in the three channels to the lowest-lying excitations of the $^{20}$Ne+$^{16}$O mass partition and the four $\alpha$-transfer channels. To study the correlated resonances for the exit channels which have the largest partial widths, summed deviation and cross correlation functions were obtained for these seven channels. Detailed discussions of the summed deviation and cross correlation functions are presented elsewhere [4,13,19]. The results are shown in Fig. 9. Three correlated structures exceed the 99% confidence limits for these two functions at $E_{\mathrm{c.m.}}=23.0$, 25.8, and 29.0 MeV. The most probable spins of these structures are $J^\pi=15^-$, $17^-$, and $19^-$, based on the angular distribution measurements discussed in the previous section.

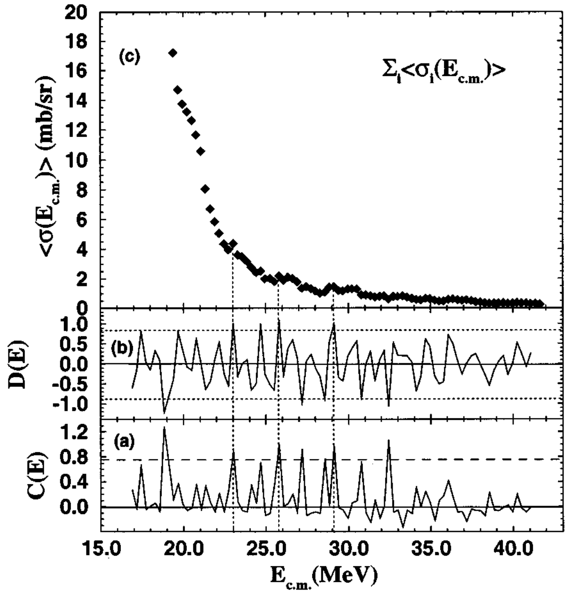

FIG. 9. Statistical analysis of selected $^{20}$Ne+$^{16}$O elastic, inelastic, and $\alpha$-transfer channels, using a square averaging interval $\Delta$ = 1.11 MeV. (a) is the cross correlation function, (b) the summed deviation function, and (c) the summed excitation function. The dashed horizontal lines represent the 99% confidence limits for statistical fluctuations in the excitation functions.

In order to illustrate the distribution of the resonance strength into the various decay channels, we will treat the angular distribution measurements at $E_{\mathrm{c.m.}}$= 20.0, 25.8, and 28.9 MeV as isolated resonances superimposed on a nonresonant background. The Breit-Wigner on-resonance cross section

$$\sigma_i = \frac{4\pi(2J+1)\Gamma_e\Gamma_i}{k^2\Gamma^2} \tag{2}$$

was used to obtain the partial widths of every reaction channel, where $\Gamma_e$, $\Gamma_i$, and $\Gamma$ are the partial widths for the elastic channel, decay channel $i$, and the total resonance width, respectively. The spin of the resonance is indicated by $J$, and $\sigma_i$ is the total resonance cross section of the corresponding decay channel. The total cross section in Eq. (2) can be extracted from the angle-averaged excitation functions by assuming an incoherent sum of the resonant and nonresonant processes. The reduced widths were also calculated for the resonances using

$$\gamma_i^2 = \frac{\Gamma_i}{2P_L(kR)}, \tag{3}$$

where $P_L(kR)$ is the Coulomb penetrability for the relevant channel at angular momentum $L$, which was obtained using the stretched spin-coupling configuration. The reduced widths were then compared with the single-particle widths $\gamma_{\mathrm{s.p.}}^2=3\hbar^2/2\mu R^2$, where $\mu$ is the exit channel reduced mass. Ratios of the reduced widths to the single-particle widths were obtained using a radius parameter $r_0=1.5$ fm. The resulting branching ratios $(\Gamma_i/\Gamma)$ and reduced widths $(\gamma_i^2/\gamma_{\mathrm{s.p.}}^2)$ for various decay channels are shown in Table III. The mass partition $^{16}$O+$^{16}$O+$\alpha$ is represented by the

TABLE III. The exit channel branching ratios for the resonances at $E_{\text{c.m.}}=20.0$, 25.8, and 28.9 MeV.

| | | $^{20}$Ne+$^{16}$O | | | $^{24}$Mg+$^{12}$C | | |
|---|---|---|---|---|---|---|---|
| $E_{\text{c.m.}}$ (MeV) | $\Gamma$ (MeV) | Channel | $\frac{\Gamma_i}{\Gamma}\times10^{-2}$ | $\frac{\gamma_i^2}{\gamma_{\text{s.p.}}^2}\times10^{-2}$ | Channel | $\frac{\Gamma_i}{\Gamma}\times10^{-2}$ | $\frac{\gamma_i^2}{\gamma_{\text{s.p.}}^2}\times10^{-2}$ |
| 28.9 | 0.83 | (g.s.,g.s.) | 3.14 | 1.84 | (g.s.,g.s.) | 0.10 | 0.04 |
| | ±0.16 | ($2_1^+$,g.s.) | 2.56 | 1.25 | ($2_1^+$,g.s.) | 1.11 | 0.38 |
| | | ($4_1^+$,g.s.) | 12.42 | 6.39 | (g.s.,$2_1^+$) | 1.83 | 0.96 |
| | | ($3_1^-$,g.s.) [a] | 3.47 | 3.25 | ($2_1^+$,$2_1^+$) | 1.30 | 0.55 |
| | | (g.s.,$0_2^+$) | 0.23 | 1.43 | | | |
| | | total | 21.82 | 14.16 | total | 4.34 | 1.93 |
| 25.8 | 0.41 | (g.s.,g.s.) | 4.22 | 1.35 | (g.s.,g.s.) | 0.38 | 0.08 |
| | ±0.07 | ($2_1^+$,g.s.) | 13.24 | 3.69 | ($2_1^+$,g.s.) | 1.83 | 0.32 |
| | | ($4_1^+$,g.s.) | 0.94 | 0.30 | (g.s.,$2_1^+$) | 3.30 | 0.95 |
| | | (g.s.,$0_2^+$) | 0.04 | 0.26 | ($2_1^+$,$2_1^+$) | 1.05 | 0.25 |
| | | total | 18.44 | 5.60 | total | 6.56 | 1.60 |
| 20.0 | 2.50 | (g.s.,g.s.) | 18.28 | 19.64 | | | |
| | ±0.27 | (g.s.,$0_2^+$) | 0.26 | 2.07 | | | |
| | | total | 18.54 | 21.71 | | | |

[a] The $^{16}$O+$^{16}$O+$\alpha$ channel.

$^{20}$Ne($3_1^-$)+$^{16}$O exit channel in the table, since $^{20}$Ne($3_1^-$) is the lowest $\alpha$-unbound excited state of $^{20}$Ne.

The resonance at $E_{\text{c.m.}}=28.9$ MeV shows a large summed branching ratio (21.82%) and reduced width ratio (14.16%) for decay into low-lying states of the $^{20}$Ne+$^{16}$O mass partition, while the branching ratio and reduced width for low-lying states of the $^{24}$Mg+$^{12}$C mass partition are much smaller, 4.34% and 1.93%, respectively. This suggests a large $^{20}$Ne+$^{16}$O component in this compound configuration. Large reduced width ratios ($\gamma_i^2/\gamma_{\text{s.p.}}^2$) for the fission channels $^{20}$Ne($4_1^+$)+$^{16}$O(g.s.) (6.42%) and $^{20}$Ne($3_1^-$, 5.62 MeV)+$^{16}$O (3.34%), both of which populate loosely $\alpha$-bound or $\alpha$-unbound states in $^{20}$Ne, suggest a structure in which a relatively free $\alpha$ particle is shared by the two $^{16}$O cores. This configuration is the only possible nearly symmetrical mass distribution in the compound system that could easily be matched by the entrance channel. Although the branching ratio for the angular momentum mismatched channel $^{20}$Ne(g.s.)+$^{16}$O($0_2^+$) is more than 10 times smaller than the well-matched channels, the reduced width of this fission channel is comparable to the two fission channels $^{20}$Ne(g.s.)+$^{16}$O(g.s.) and $^{20}$Ne($2_1^+$)+$^{16}$O(g.s.). This fact suggests that the molecular resonance formation mechanism is important for the magnitude of the cross sections observed in the $^{20}$Ne(gs)+$^{16}$O($0_2^+$) channel. The spin value of this resonance is two to three units of $\hbar$ larger than the grazing angular momentum of the $^{20}$Ne(g.s.)+$^{16}$O($0_2^+$) channel at this energy (assuming spherical nuclear shapes). This mismatch could be compensated for by the deformation of the $^{16}$O($0_2^+$) state if the nucleus were aligned along its major axis relative to the $^{20}$Ne fragment. This would help to support the large angular momentum of the entrance channel, something that is critical to its ability to share this resonance with other channels. The decay parameters for the resonance at $E_{\text{c.m.}}=25.8$ MeV show that the reduced width ratio is 1.60% for decay into low-lying states of the $^{24}$Mg+$^{12}$C mass partition, while it is 5.60% for the $^{20}$Ne+$^{16}$O mass partition. Therefore the decay from this resonance is also dominated by the $^{20}$Ne+$^{16}$O mass partition. The broad structure centered at $E_{\text{c.m.}}=20.0$ MeV observed in the $^{20}$Ne(g.s.)+$^{16}$O($0_2^+$) channel is also treated as an isolated resonance. As seen in Table III, the reduced widths for decay into the elastic channel and the inelastic $^{20}$Ne(g.s.)+$^{16}$O($0_2^+$) channel are about 20% and 2% of the single-particle width, respectively. The reduced width of this resonance for decay into the angular momentum mismatched $0_2^+$ channel is larger than those from the 17$\hbar$ and 19$\hbar$ states. This fact may be due to the resonance spin $J=6\hbar$, which is closer to the grazing partial wave of the exit channel than to that of the entrance channel.

As was discussed in the Introduction, a superdeformed configuration in $^{36}$Ar has been predicted using the cranked cluster model [8]. The resulting rotational band is characterized by a $^{16}$O-$\alpha$-$^{16}$O colinear alignment with a 3:1 major-to-minor axis ratio. A comparison between the current results and the results of those calculations is shown in Fig. 10. The vertical scale in Fig. 10 indicates the energy relative to the breakup threshold for $^{16}$O+$^{16}$O+$\alpha$. The three crosses represent the tentative spin assignments of the statistically significant correlated resonances at $E_{\text{c.m.}}=23.0$, 25.8, and 29.0 MeV observed in the current experiment. The general energy versus spin dependence of these resonances suggests they are members of a single rotational band of the compound system, which has a moment of inertia similar to that predicted by Rae and Merchant [8]. However, the energies of the states observed in the current work are about 10 MeV larger than those calculated by the cranked cluster model, and all have negative parity. The additional excitation energy for these resonances relative to the results of Ref. [8] might be a consequence of the negative parity.

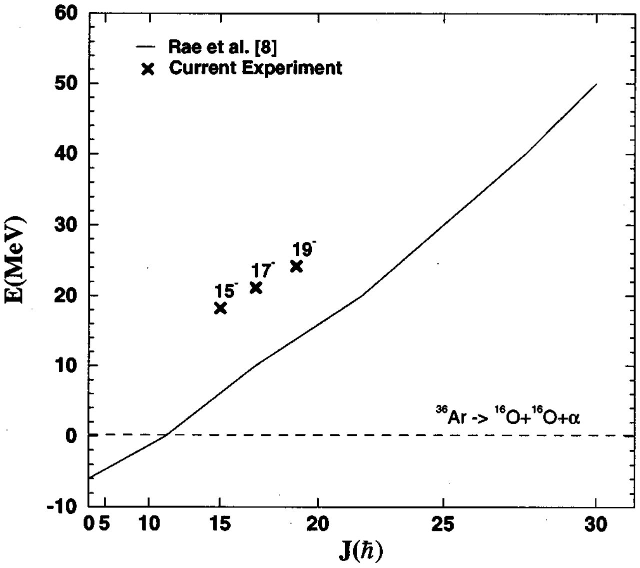

FIG. 10. A comparison of the spin versus breakup energy dependence of the spin assignments from this work with the results of a cranked cluster model calculation [8] for $^{36}$Ar.

## V. SUMMARY

We have reported excitation functions of $^{20}\mathrm{Ne}+{}^{16}\mathrm{O}$ for both the $^{20}\mathrm{Ne}+{}^{16}\mathrm{O}$ and $^{24}\mathrm{Mg}+{}^{12}\mathrm{C}$ mass partitions. Various resonant structures are present in both partitions. Three statistically significant correlated structures have been identified at $E_{\mathrm{c.m.}}=23.0$, 25.8, and 29.0 MeV, although none of them is common to all the excitation functions studied in this work. The strongest correlations are in the elastic channel, the low-lying inelastic channels ($|Q|\leqslant 6.05$ MeV), and the four $\alpha$-transfer channels. The tentative spin assignments suggest that these resonances correspond to members of a single rotational band with negative parity. Most likely these resonances are not the rotational states predicted by the cranked cluster calculations, which have symmetrical mass distributions and positive parity.

The negative parity of the spins assignments in this work represents a fundamental departure from the results of Schimizu *et al.* [6], in which the majority of the spin assigments were even, positive parity. As was discussed in the Introduction, the measurements of Schimizu *et al.* [6] were single-angle excitation functions ($\theta_{\mathrm{lab}}=13°$). In the angle-averaged excitation functions of the current work, the resonances reported in Ref. [6] are either much weaker relative to the background or not visible at all. None of the centroid energies for the resonances reported in Ref. [6] corresponds to a correlated resonance in the current work.

It is possible that a large entrance channel prolate deformation for both reactants is not a necessary condition to populate highly deformed excited states in $^{36}$Ar, since in this system a highly deformed shape can be accomplished through a loosely bound $\alpha$ particle positioned between the two $^{16}$O cores. However, the deformation of the $^{16}\mathrm{O}(0_2^+)$ state may increase the partial width for decay into the $^{20}\mathrm{Ne}+{}^{16}\mathrm{O}(0_2^+)$ channel. The elastic angular distribution measurements demonstrate the importance of the $\alpha$-transfer process at large angles for the nonresonant background processes, and are consistent with the results of a previous study [5].

## ACKNOWLEDGMENTS

We would like to acknowledge the assistance of R. Antonov, X. Li, and D. Essiam during data acquisition. We would like to thank H. T. Fortune and Z. Mao for helpful discussions. This work was supported by the National Science Foundation.

---

[1] R. W. Zurmühle, P. Kutt, R. R. Betts, S. Saini, F. Haas, and O. Hansen, Phys. Lett. **129B**, 384 (1983).
[2] A. H. Wuosmaa, R. W. Zurmühle, P. Kutt, S. F. Pate, S. Saini, M. L. Halbert, and D. C. Hensley, Phys. Rev. C **41**, 2666 (1990).
[3] S. P. Barrow, R. W. Zurmühle, J. T. Murgatroyd, N. G. Wimer, Y. Miao, K. R. Pohl, A. H. Wuosmaa, R. R. Betts, M. Freer, and B. Glagola, Phys. Rev. C **51**, 1961 (1995).
[4] S. P. Barrow, R. W. Zurmühle, D. R. Benton, Y. Miao, Q. Li, P. H. Kutt, Z. Liu, C. Lee, N. G. Wimer, and J. T. Murgatroyd, Phys. Rev. C (to be published).
[5] M. Gai, G. M. Berkowitz, P. Braun-Munzinger, C. M. Jachcinski, C. E. Ordoñez, T. R. Renner, and C. D. Uhlhorn, Phys. Rev. C **30**, 925 (1984).
[6] J. Schimizu, W. Yokota, T. Nakagawa, Y. Fukuchi, M. Sato, S. Hanashima, Y. Nagashima, K. Furuno, and K. Katori, Phys. Lett. **112B**, 323 (1982).
[7] R. M. Freeman, F. Haas, B. Heusch, and S. M. Lee, Phys. Rev. C **20**, 569 (1979).
[8] W. D. M. Rae and A. C. Merchant, Phys. Lett. B **279**, 207 (1992).
[9] J. Zhang, W. D. M. Rae, and A. C. Merchant (unpublished).
[10] S. Marsh and W. D. M. Rae, Phys. Lett. B **180**, 185 (1986).
[11] S. P. Barrow, R. W. Zurmühle, A. H. Wuosmaa, and S. F. Pate, Phys. Rev. C **46**, 1934 (1992).
[12] Micron Semiconductor Limited, Sussex BN15 8UN, England.
[13] Y. Miao, Ph.D. thesis, University of Pennsylvania, 1995.
[14] W. K. Wells, D. Cebra, and D. P. Balamuth, Nucl. Instrum. Methods **223**, 103 (1984).
[15] N. Wimer, Ph.D. thesis, University of Pennsylvania, 1994.
[16] S. Zawadski, computer code ABACUS (private communication).
[17] P. D. Kunz, computer code DWUCK5 (private communication).
[18] R. Stock, U. Jahnke, D. L. Hendrie, J. Mahoney, C. F. Maguire, W. F. W. Schneider, D. K. Scott, and G. Wolschin, Phys. Rev. C **14**, 1824 (1976).
[19] S. Saini and R. R. Betts, Phys. Rev. C **29**, 1769 (1984).